Water Resources Research

RESEARCH ARTICLE
10.1029/2023WR036539

Quantifying Aspect-Dependent Snowpack Response to High-Elevation Wildfire in the Southern Rocky Mountains

Wyatt Reis[1,2], Daniel McGrath[1], Kelly Elder[3], Stephanie Kampf[4], and David Rey[5]

[1]Department of Geosciences, Colorado State University, Fort Collins, CO, USA, [2]Cold Regions Research and Engineering Laboratory, Engineering Research and Development Center, Hanover, NH, USA, [3]Rocky Mountain Research Station, United States Forest Service, Fort Collins, CO, USA, [4]Department of Ecosystem Science and Sustainability, Colorado State University, Fort Collins, CO, USA, [5]United States Geological Survey, Observing Systems Division, Denver, CO, USA

Key Points:

- The burned south site reached peak snow water equivalent 22 days earlier than all other sites, which peaked simultaneously
- Burned site melt rates were similar across aspects but exceeded unburned sites by ~9 mm d^{-1}, causing snow disappearance ~9 days earlier
- Burned site net energy balance was dominated by longwave radiation losses in winter and shortwave radiation gains in spring

Supporting Information:

Supporting Information may be found in the online version of this article.

Correspondence to:

W. Reis and D. McGrath,
wyatt.k.reis@usace.army.mil;
daniel.mcgrath@colostate.edu

Citation:

Reis, W., McGrath, D., Elder, K., Kampf, S., & Rey, D. (2024). Quantifying aspect-dependent snowpack response to high-elevation wildfire in the Southern Rocky Mountains. *Water Resources Research*, *60*, e2023WR036539. https://doi.org/10.1029/2023WR036539

Received 23 OCT 2023
Accepted 24 AUG 2024

Abstract Increasing wildfire frequency and severity in high-elevation seasonal snow zones presents a considerable water resource management challenge across the western United States (U.S.). Wildfires can affect snowpack accumulation and melt patterns, altering the quantity and timing of runoff. While prior research has shown that wildfire generally increases snow melt rates and advances snow disappearance dates, uncertainties remain regarding variations across complex terrain and the energy balance between burned and unburned areas. Utilizing paired in situ data sources within the 2020 Cameron Peak burn area on the Front Range of Colorado, U.S., during the 2021–2022 winter, we found no significant difference in peak snow water equivalent (SWE) magnitude between burned and unburned areas. However, the burned south aspect reached peak SWE 22 days earlier than burned north. During the ablation period, burned south melt rates were 71% faster than unburned south melt rates, whereas burned north melt rates were 94% faster than unburned north aspects. Snow disappeared 7–11 days earlier in burned areas than unburned areas. Net energy differences at the burned and unburned weather station sites were seasonally variable, the burned area snowpack lost more net energy during the winter, but gained more net energy during the spring. Increased incoming shortwave radiation at the burned site was 6*x* more impactful in altering the net shortwave radiation balance than the decline in surface albedo. These findings emphasize the need for post-wildfire water resource planning that accounts for aspect-dependent differences in energy and mass balance to accurately predict snowpack storage and runoff timing.

Plain Language Summary Wildfires are burning more frequently at high-elevations, where they modify the snowpack. This complicates efforts to predict when snowmelt runoff will occur and the amount of water that will melt from the snowpack. Wildfire generally causes snow to melt earlier in the year and at a faster rate. However, in complex, mountainous terrain, it is not well understood how the magnitude of these changes may differ between neighboring slopes. During the 2021–22 winter in the Cameron Peak burn area (2020) in Colorado, we found that in a high-elevation snowpack there was no difference in the amount of water accumulated in the snowpack between areas that were burned by the fire and areas that were not. But in areas that burned, the amount of water in the snowpack reached its largest amount 22 days earlier than the areas that did not burn. The snowpack melted faster on both south and north facing slopes in the burned area than comparable unburned areas, causing the burned areas to be snow free 7–11 days earlier. These results highlight the need to account for complex terrain in water resource planning.

1. Introduction

Across North America, 60% of seasonal snow accumulates in mountainous regions, causing distinct seasonal hydrologic cycles in snow-dominated watersheds (Bales et al., 2006; Wrzesien et al., 2018). For these basins, 60%–80% of spring and summer streamflow is derived from liquid water stored in seasonal snowpacks (Li et al., 2017). Consequently, quantifying seasonal snow accumulation and ablation dynamics can help inform the management of downstream water supplies, hydropower generation, and agricultural production (Barnett et al., 2005; Li et al., 2017; Sturm et al., 2017; Viviroli et al., 2007). However, over the last century, 1 April SWE has declined by ~20% across the western United States (U.S.) (Mote et al., 2005, 2018). In the last 50 years, melt has initiated 1–3 weeks earlier (Cayan et al., 2001; Clow, 2010; Dudley et al., 2017; Hall et al., 2015; McCabe & Clark, 2005; Wagner et al., 2021) resulting in reduced melt rates, increased evapotranspiration, and reduced runoff generation (Barnhart et al., 2016; Musselman et al., 2017). Additionally, the hydrology within snow-dominated watersheds is bifurcating based on elevation. In the Upper Colorado River Basin, for example,

areas below ~3,300 m are predicted to dramatically decline in peak SWE (14%–45%) while peak SWE at higher elevations will remain unchanged (Hammond et al., 2023).

The changing timing and increased proportion of rain and earlier snowmelt/spring runoff within these snow-dominated watersheds can reduce water storage and soil moisture, increasing the potential for wildfire activity during subsequent summers (Hale et al., 2023; Hammond et al., 2023; O'Leary III et al., 2019; Westerling, 2016). Additionally, a history of fire suppression in the western U.S., has led to a rapid growth in wildfire burn area, greater fire severity, and higher median elevation of wildfires over the last half-century, with an additional pronounced increase since the early 2000s (Alizadeh et al., 2021; Iglesias et al., 2022; Shi & Touge, 2023; Westerling et al., 2006). Between 1984 and 2017, western U.S. forests above 2,500 m experienced a 270% increase in wildfire activity, with the median burned elevation increasing by 250 m (Alizadeh et al., 2021). Model projections indicate a 63%–107% increase in mean annual wildfire burn area by the end of the century (Alizadeh et al., 2021; Mueller et al., 2020; Westerling et al., 2011). The expansion of wildfire into high-elevation forests has preferentially impacted late season snow zones (typical snow free date after 15 April), with 70% of western U.S. ecoregions experiencing a significant increase in burned area within these snow zones (Kampf et al., 2022).

High-elevation forests regulate the accumulation and melt of seasonal snowpacks by altering wind speed, precipitation, and energy fluxes (Elder et al., 1989, 1991; Liston et al., 2007; Roth & Nolin, 2017; Trujillo et al., 2007). Thus, disturbances by wildfire have the potential to alter the mass and energy balances of snow-dominated watersheds. There are four primary forest disturbances that affect snowpacks following wildfire. They include: a reduction in canopy, which leads to (a) less snowfall interception (Harpold et al., 2014; McGrath et al., 2023) and (b) an increase in shortwave radiation reaching the snow surface (Burles & Boon, 2011), (c) a lower snow surface albedo from the accumulation of soot/burned debris (Gleason & Nolin, 2016; Gleason et al., 2013; Uecker et al., 2020), and (d) increases in turbulent fluxes because of higher wind speeds due to the more open forest structure (Boon, 2009; Molotch et al., 2009). In most seasonal snow burned areas, these competing changes to the mass and energy balances decrease peak SWE while increasing melt rates (Giovando & Niemann, 2022; Loiselle et al., 2020; Maina & Siirila-Woodburn, 2020; Smoot & Gleason, 2021), yet the hydrological and snow characteristics impacts vary between ecoregions, as well as across snow zones (e.g., early vs. late) (Giovando & Niemann, 2022; Kampf et al., 2022). Further, the loss of forest canopy due to disturbance (e.g., wildfire, drought, and disease) can both increase or decrease summertime evapotranspiration and runoff due to variability in water and energy limits between ecoregions (Goeking & Tarboton, 2020, 2022).

While a consensus is emerging on the primary impacts of wildfire on snow, prior work has not thoroughly evaluated how these impacts might vary across the complex topography that characterizes high-elevation mountain environments in the western U.S. Furthermore, few studies have assessed how the changes in forest structure post-fire influence all components of the snowpack energy balance. Our work addresses these two key questions and knowledge gaps:

1. How does complex terrain modulate wildfire impacts on snowpack characteristics (e.g., peak SWE magnitude and timing, snowmelt rates and snow-free dates)?
   Aspect exerts a strong control on peak SWE and melt patterns of seasonal snowpacks (e.g., Anderson et al., 2014; Elder et al., 1991), but most previous post-wildfire snowpack studies have not focused on identifying the way changes in quantity and timing of peak SWE, and melt rates are modulated by complex terrain in wildfire burned areas. In the limited number of studies that incorporated differences in aspect, the greatest declines in snow depth and advances in snow disappearance dates occurred on south-facing slopes (Maxwell et al., 2019; Moeser et al., 2020).

2. How is the snowpack energy balance altered following wildfire?
   Prior studies have consistently attributed the observed increases in melt rates post-fire to an increase in shortwave radiation reaching the snow surface and a decrease in snow surface albedo (Burles & Boon, 2011; Gleason et al., 2013; Harpold et al., 2014). However, the other components (longwave radiation, turbulent fluxes) of the energy balance have not been systematically assessed post-fire.

We address these knowledge gaps using multiple sources of data including bi-weekly manual snowpack observations and two continuous automatic weather stations paired across aspect and burn condition in the Cameron Peak burn scar, Colorado, during the 2021–22 winter.

2. Study Site

We established a study area at an elevation of ∼3,050 m within the sub-alpine zone of the Cache la Poudre watershed approximately 5 km north of Cameron Pass in northcentral Colorado (Figures 1a and 1b). The 2 km^2 study area is situated in a mixed forest of subalpine fir (Abies lasiocarpa), Douglas fir (Pseudotsuga menziesii), and Engelmann spruce (Picea engelmannii) and is within the persistent seasonal snow zone (SSZ) (Moore et al., 2015). The study area location allowed us to sample the range of burn severities present in the burned SSZ, but given the burn conditions in the study area, oversampled high-burn severities and under sampled low-to moderate burn severities relative to their distribution in the fire as a whole (Figure 1f). Similarly, the study site spanned the range of northness values (defined below) present within the burned SSZ (Figure 1g).

In the study area, we installed an automated weather station (AWS) in January 2021 in a high burn severity location (Burned—AWS; Figure 1). In November 2021, we installed an additional AWS in a ∼5 m by 5 m forest gap representative of unburned forests in the area (Unburned—AWS). Additionally, we measured snow depth at an under-canopy location (Unburned—UC) with an automated sonic snow depth sensor. These three sites have comparable southeast aspects with northness values ranging between −0.12 and 0.02 and slope angles between 2.8 and 6.3° (Table 1). In November 2021, we established three additional sites to measure snow depth with time-lapse cameras and snow depth poles on sloped terrain (Burned—North, Burned—South, Unburned—North: Table 1; Figures 1b and 1c). We also established four ∼500 m snow depth transects in November 2021 that covered a range of aspects in burned and unburned locations (Figures 1b and 1c). For this analysis, we focus only on data from November 2021 to June 2022.

The Joe Wright Snow Telemetry (SNOTEL) site (ID 551) is located about 80 m higher in elevation and 3.5 km southwest of the main study area. During the 2021–2022, the SNOTEL site recorded a peak SWE of 632 mm on 10 May. The 30-year normal peak SWE of the station is 622 mm on 6 May. Snow disappearance at the site occurred on 15 June 2022, just 2 days earlier than the 17 June 30-year median snow disappearance date (SDD).

3. Materials and Methods

3.1. Automated Weather Stations

The burned and unburned AWS measure air temperature and relative humidity *(Campbell Scientific HydroVUE5),* snow depth (*Campbell Scientific SR*50A), snow/soil temperature and relative permittivity *(Campbell Scientific SoilVUE10; unburned,* 1 m *length; burned, 0.*5 m *length)*, wind speed and direction *(RM Young 05103 Wind Monitor)*, barometric pressure *(Campbell Scientific CS100; burned only),* and four-component net radiation *(Apogee SN500SS)*. The four-component net radiometer had a spectral range of 385–2105 nm (upward-looking) and 295–2685 nm (downward-looking). The AWS sites were programmed to collect data every minute and logged the 15 minute and hourly mean values. The UC site was instrumented with a standalone sonic snow depth sensor *(A2 Photonic Sensors SPICE)*.

We also measured snow depth at the two AWS sites and at three additional snow depth sites using time-lapse cameras (*Wingscapes TimelapseCam Pro*) and snow depth poles with 10 cm gradation (Figure S1f in Supporting Information S1). We installed three snow depth poles at the time-lapse camera sites without a weather station and one pole at the AWS sites. We programmed the time-lapse cameras to capture an hourly photo between 0700 and 1900. Using the photos from noon (1200) or the next interpretable photo, we manually recorded daily snow depths with 5 cm precision and calculated the average daily snow depth for the site.

3.2. Manual Snowpack Measurements

From 14 Novembe to 13 June, we collected snow pit and snow depth transect data approximately every other week. The snow pit observations were co-located with the two AWS and three time-lapse camera sites and included vertical profiles (10 cm increments) of snow density, dielectric permittivity, and temperature, as well as snow stratigraphy, and grain size profiles by layer. Pits were dug with the measurement wall facing north and the thermometer was shaded with a shovel to minimize the influence of direct solar radiation on the surface and near-surface measurements. We dug the snow pits in the same general location each time but shifted them ∼1 m behind the previous pit wall and backfilled the pits following data collection to minimize the influence of the previous pit face on the following data collection.

10.1029/2023WR036539

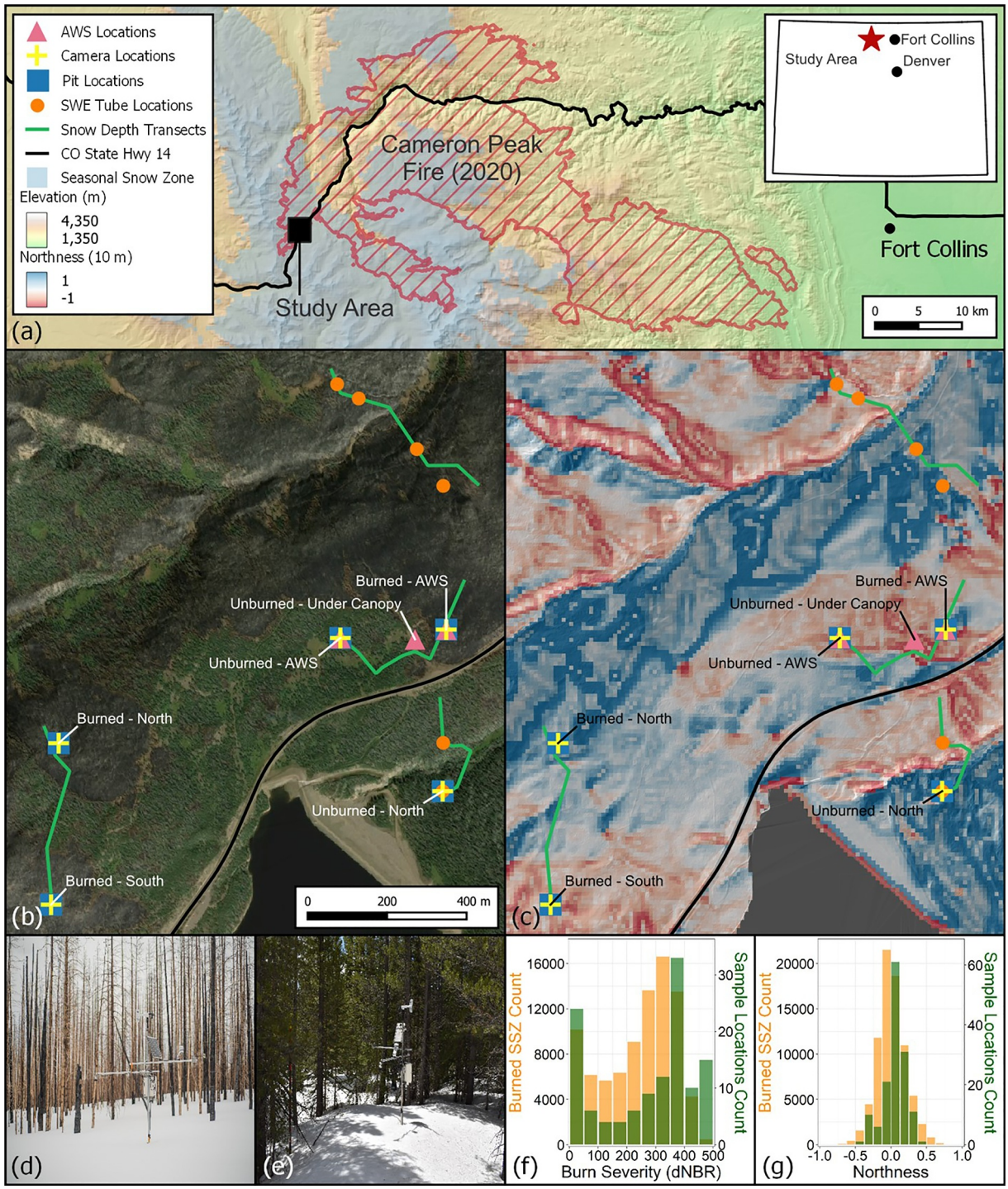

Figure 1. (a) Study area location within 2020 Cameron Peak wildfire burn area and the persistent seasonal snow zone (SSZ) (Moore et al., 2015). (b) Maxar optical imagery of the study with study site locations overlaid. (c) Northness (10 m resolution) for the study area. (d) Burned-area automated weather station (AWS). (e) Unburned-area AWS. (f) Histogram of binned differenced normalized burn ratio (dNBR) within the SSZ impacted by the Cameron Peak fire (orange) and the repeat snow depth transect locations (green). On the dNBR scale, moderate–low severity burn values range from 270 to 439 and moderate–high burn severity values are between 440 and 659. (g) Histogram of northness values within the burned SSZ (orange) and the sampled locations (green). Northness values greater than 0 are north-facing, while values less than 0 are south-facing.

Table 1
Study Site Locations, Difference Normalized Burn Ratios (Dnbr), Elevations, and Topographic Characteristics

Site name	Coordinates (degrees)	dNBR (Unitless)	Elevation (m a.s.l.)	Aspect (deg)	Slope (deg)	Northness (−1 to 1)
Burned—AWS	(40.564, −105.867)	373	3,009	65	2	0.02
Burned—North (Camera)	(40.561, −105.879)	355	3,095	40	13	0.16
Burned—South (Camera)	(40.558, −105.879)	464	3,102	220	20	−0.26
Unburned—AWS	(40.563, −105.870)	–	3,019	175	7	−0.12
Unburned—North (Camera)	(40.560, −105.867)	–	2991	15	24	0.39
Unburned—Under-Canopy (UC)	(40.564, −105.868)	–	3,010	170	5	−0.08

Snow depths along each of the four transects were collected during the same week as snow pit observations. Snow depths were measured using a 3 m Snowmetrics probe with 1 cm gradations and taken in a 1 m five-point "plus sign" pattern (Harpold et al., 2014), every ∼15 m along the transects. Each measurement was geolocated using a Juniper Systems Geode GNSS receiver (<30 cm horizontal accuracy), allowing us to collect snow depth in repeat locations throughout the winter. Mean snow depth for each location was calculated using the five snow depths and slope, aspect, and burn condition was assigned to each location based on the post-fire 2021 lidar-derived DEM (0.7 m resolution) and the post-fire difference Normalized Burn Ratio (dNBR) burn severity map. We subsequently refer to these distributed measurements as "probe-derived." While completing snow depth transects, bulk snowpack density measurements were also collected using a Snow-Hydro SWE Coring Tube at six locations (Figures 1b and 1c).

3.3. Snow Surface Albedo Measurements

To reduce noise in the unburned AWS shortwave radiation data, we calculated daily albedo from median hourly values between 10:00 and 14:00 each day and applied a 7-day median smoothing function at both weather stations.

Spectral albedo observations were also collected in the burned forest and an open unburned meadow near the burned and unburned AWS sites under clear-sky conditions on 15 May. We used a Malvern Panalytical/Analytical Spectral Devices (ASD) FieldSpec 4 Standard-Res spectroradiometer (3 nm VNIR, 10 nm SWIR resolution) at six locations evenly split between the burned and the unburned areas near the AWS sites. At each of the locations, five upwelling and five downwelling measurements were taken within 2 hr of solar noon using the ASD remote cosine reflector on an outstretched 60 cm metal arm to the south of a tripod. Each of the five manually triggered observations collected five automated measurements. Albedo was calculated as the ratio of the mean upwelling and downwelling radiation measurements and is presented here as the mean spectral albedo at the burned and unburned sites.

3.4. Snow Water Equivalent Calculations

Using the density profiles from each snow pit, we calculated the bulk snow density. Combining the bulk pit densities with density from the six SWE tube locations, we calculated the mean density for each aspect and burn condition. Bulk snowpack density was then linearly interpolated between sampling dates to attain an estimate of daily bulk density. Mean daily SWE was calculated for each aspect and burn condition by multiplying the daily bulk density by the probe depth measurements. The mean SWE was then calculated for each aspect and burn condition by grouping the sites by aspect and burn condition. Mean continuous SWE measurements were calculated for each burn condition and aspect using the continuous snow depth measurements from the time-lapse cameras and sonic snow depth sensors. To calculate the SWE, we applied the linearly interpolated snow densities by burn condition and site aspect. These continuous sites will be referred to as "continuous SWE."

3.5. Terrain and Cold Content Analysis

As a measure of terrain aspect, we calculated northness (Molotch et al., 2005),

$$\text{Northness} = \cos(\text{aspect } (^\circ)) \times \sin(\text{slope angle } (^\circ)) \quad (1)$$

To determine the slope angle and topographic aspect at each point, we used a combination of the USGS LiDAR-derived DEM with a 0.7 m spatial resolution and the USGS DEM with 10 m spatial resolution. We combined resolutions since the slope values in the 10 m DEM were not realistic for our study site, but the 10 m DEM was needed to reduce noise and accurately capture site aspects. Using the two rasters, we calculated the northness at a 0.7 m spatial resolution for all analyses but are showing a down-sampled 10 m resolution northness rater in Figure 1 to improve readability.

Cold content is a measure of the snowpack energy deficit, which depends on the snowpack's temperature and mass. This deficit must be overcome before snowmelt runoff can occur. We calculated cold content for each study site as:

$$CC = c_i \rho_s d_s (T_S - T_m), \tag{2}$$

where CC is the snowpack cold content (MJ m^{-2}), c_i is the specific heat of ice (2.1×10^{-3} MJ $kg^{-1}°C^{-1}$), ρ_s is the density of snow (kg m^{-3}), d_s is snow depth (m), T_S is the depth weighted snowpack temperature (°C), and T_m is the melting temperature of snow (0°C). To be more representative of the study area, we calculated cold content using the median probe snow depth in each burn condition (burned/unburned) and aspect (north/south) instead of using the snow pit depth.

3.6. Snowpack Energy Balance Analysis

Using the AWS station observations at both the burned and unburned AWS sites, we calculated the total energy using a simple one-dimensional (vertical) model:

$$Q = K + L + H + L_v E + R + G \tag{3}$$

where Q is the total energy available, K is the net shortwave radiation, L is the net longwave radiation, H is the sensible heat flux, and $L_v E$ is the latent heat flux. The energy inputs from rainfall (R) and the ground heat flux (G) were not included since no rain was observed during the observational period, and the ground heat flux is assumed to be negligible (Boon, 2009). All terms have units of W m^{-2}.

3.6.1. Shortwave and Longwave Radiation

For each site, we calculated K and L from the mean hourly observations using:

$$K = K_{\text{in}} - K_{\text{out}} \tag{4}$$

and,

$$L = L_{\text{in}} - L_{\text{out}} \tag{5}$$

where K_{in} and L_{in} are the incoming radiation components (W m^{-2}), while K_{out} and L_{out} are the outgoing radiation components (W m^{-2}). Hours with incoming shortwave radiation values less than outgoing shortwave radiation were removed since these are not physically realistic and are likely due to snow covering the upward-looking sensor. As a result, for days with less than 6 hr of recorded shortwave data, we did not calculate the other energy balance components for that day at the site ($n = 17$; Figure S2 in Supporting Information S1).

3.6.2. Turbulent Energy Flux Modeling

We measured wind speed at two locations, the burned AWS and the unburned AWS. Wind speed and air temperature were measured 3 m above the ground surface at the burned and unburned sites. We logarithmically extrapolated wind speeds and linearly extrapolated air temperatures down to the height of the snow surface to calculate the sensible and latent heat fluxes (Boon, 2009; Mandal et al., 2022).

For each of the sites, hourly H and $L_v E$ were calculated as a function of the temperature, vapor pressure, and wind speed gradients above the surface of the of the snow,

$$H = \rho_a C_p D_H (T_a - T_{ss}), \tag{6}$$

$$L_v E = \rho_a \lambda_v D_E \frac{0.622}{10 P_a} (e_a - e_s), \tag{7}$$

where ρ_a is the air density at the sites (kg m^{-3}),

$$\rho_a = \frac{0.34722 \times P_a}{T_a}, \tag{8}$$

where P_a is the air pressure (mbar) at each site. Since air pressure was only recorded at the burned AWS and both sites are within 500 m of each other and at similar elevations, the burned AWS air pressure was used at both sites. The specific heat capacity of air (C_p) was set as 1,005 J kg^{-1} K^{-1}. T_a is the air temperature (°K) and the snow surface temperature (T_{ss}; °K) was calculated using,

$$T_{ss} = \left(\frac{L_{out}}{\varepsilon_s \sigma}\right)^{\frac{1}{4}}, \tag{9}$$

where the emissivity (ε_s) of the snow surface is assumed to be 0.97 (Hardy et al., 1997), and σ is the Stefan-Boltzmann constant (5.67 × 10^{-8} W m^{-2} K^{-4}). Comparing the calculated T_{ss} values from Equation 9 to the measured snow surface temperatures from each snow pit, we identified that the calculated T_{ss} values were consistently warmer (difference ranged from −1.0–+ 6.1°C) than the measured values at both the burned and unburned AWS sites (Figure S3 in Supporting Information S1). The error between the measured and calculated varied between the two burn conditions and with time of year. To correct for this error, we calculated the median error at each site before and after 1 March, then subtracted the median error from the calculated T_{ss} value based on the date (Table S1 in Supporting Information S1).

The latent heat of vapourization (λ_v; MJ kg^{-1}) was given by,

$$\lambda_v = 2.501 - 0.002361(t_{ss}), \tag{10}$$

where t_{ss} is the snow surface temperature in degrees Celsius.

Using Teten's formula (Murray, 1967), we calculated the saturation vapor pressure of the air ($e_{a_{sat}}$) and the snow surface ($e_{s_{sat}}$) in kPa,

$$e_{a_{sat}} \; or \; e_{s_{sat}} = \begin{cases} 6.11 \times \exp\left(\dfrac{17.27 t_{a\ or\ ss}}{t_{a\ or\ ss} + 237.3}\right); & t_{a \text{ or } ss} > 0℃ \\ 6.11 \times \exp\left(\dfrac{21.87 t_{a\ or\ ss}}{t_{a\ or\ ss} + 265.5}\right); & t_{a \text{ or } ss} \le 0℃ \end{cases}, \tag{11}$$

where $t_{a\ or\ ss}$ is either the air temperature (t_a) or snow surface temperature (t_{ss}) in degrees Celsius. We assumed the snow surface vapor pressure (e_s) was always saturated, giving $e_s = e_{s_{sat}}$, but to determine the air vapor pressure (e_a), we used,

$$e_a = \frac{RH}{100\%} \times e_{a_{sat}}, \tag{12}$$

where RH is the hourly measured relative humidity (%) at each AWS site.

Finally, D_H and D_E are the bulk transfer coefficients of sensible and latent heat (m s^{-1}). Under neutral atmospheric conditions, D_H and D_E are assumed to be equivalent to each other and calculated as:

$$D_H = D_E = \frac{k^2 u}{\left[\ln\left(\frac{z_u}{z_0}\right)\right]^2}, \tag{13}$$

where k is the von Karman constant (0.4) and z_0 is the roughness length (m). Due to a lack of field measurements, we assumed all roughness lengths to be 0.006 m following Boon (2009). The wind speed measurement height (z_u) is the time-varying height (m) above the snowpack surface at each site.

To account for the stability of the surface boundary layer and correct the turbulent fluxes under highly variable conditions we used the Richardson number (R_i) (Brutsaert, 1982):

$$R_i = g\frac{(T_a - T_{ss})\ z_u}{T_a u^2}, \tag{14}$$

where g is gravitation acceleration (9.81 m s^{-2}), u is the hourly average wind speed (m s^{-1}) measured at each site. Due to substantial variability, potential hysteresis, and a wide-range in published values and approaches in the determination of the R_i critical number (Andreas, 2002), turbulence was dampened when R_i was outside the range of −0.4 and 0.3 (Andreas, 2002; Boon, 2009; Mandal et al., 2022). The turbulence was dampened for stable atmospheric conditions using,

$$D_{H_C} = D_{E_C} = \frac{D_H}{(1 + 10R_i)}. \tag{15}$$

3.7. Summary of Methods

To quantify how complex terrain modulates the impacts of wildfire on high-elevation snowpacks, we use the distributed, but periodic in situ data to address our first research question related to snowpack characteristics (magnitude and date of peak SWE, melt rates and snow-free dates). Statistical differences between the burned and unburned site were identified using the Wilcoxon t-test. To address our second research question, we use the paired burned and unburned AWS data to quantify how components of the seasonal snowpack energy balance differed between burned and unburned sites.

4. Results

Wildfires fundamentally alter canopy and forest structure, leading to significant impacts on the snowpack mass and energy balance. Here, we first identify differences in snowpack characteristics, and then quantify the full snowpack energy balance to help explain differences in the burned and unburned snowpacks throughout the winter and spring.

4.1. Aspect Influence on Snowpack Characteristics

4.1.1. Quantity and Timing of Peak SWE

Our measurements fall into four categories based on aspect (north, south) and burn condition (burned, unburned). Bulk snowpack density from snow surveys exhibited similar temporal trends on all aspects throughout the observation period (Figure 2a). Snowpack density at the burned and unburned sites were comparable across aspects, but burned site snow densities were greater on average (~10% greater on north-facing slopes and ~15% greater on south-facing slopes).

The median SWE of the probe transects was greater on both north and south aspects in the burned area relative to the same aspect in the unburned area for each probe survey throughout the accumulation period except for 28 November and 28 December on south aspects (Figures 2b and 2c). However, median probe-derived SWE was only significantly different (Wilcoxon t-test; $p < 0.05$) between burned and unburned areas for one survey date on north aspects and four survey dates on south aspects during this period (Figures 2b and 2c). Median probe-derived SWE was significantly greater ($p < 0.05$) on north aspects relative to south aspects in both the burned (54% greater SWE) and unburned (59% greater SWE) areas. Additionally, we found the difference in median

10.1029/2023WR036539

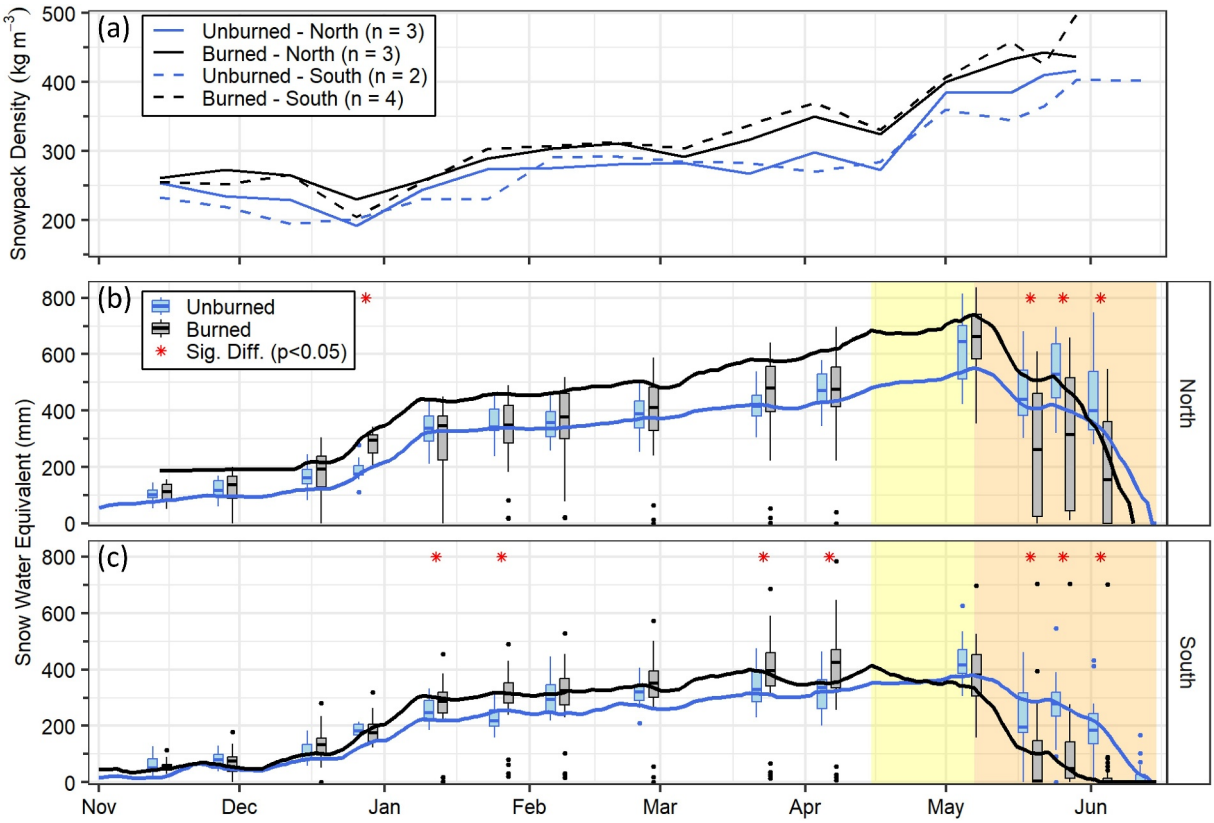

Figure 2. (a) Mean density for each aspect and burn condition calculated from the snow pit and snow water equivalent (SWE) tube bulk densities. The number of sites included for each aspect and burn condition is indicated in the legend. Probe-derived (box and whisker) and continuous (line) SWE based on burn condition for (b) north and (c) south aspects. Wilcoxon significant difference of medians between burned and unburned areas are indicated with the red asterisks ($p < 0.05$). The period between burned south peak SWE (15 April) and all other sites peak SWE (7 May) is shown in yellow. The melt period for all sites is shown in orange. Note: Burned-north SWE until mid-December is based on snow pit observations only.

interquartile range (IQR) of probe-derived SWE was significantly greater ($p < 0.05$) on north burned aspects relative to north unburned areas, and on north aspects compared to south aspects within the burned area during the accumulation period.

For most aspect/burn categories, the AWS and camera-derived SWE was comparable to the median probe-derived SWE measurements during the accumulation period (less than 13% median absolute difference). The one exception was the burned north aspect (camera) site which consistently had greater SWE (25% median absolute difference), likely due to preferential wind deposition and the persistence of early season snow at this site (Figures 2b and 2c).

The burned south aspect camera site (Burned–South Camera) reached peak SWE on 15 April, 22 days earlier than the other four sites (Burned–North Camera, Burned AWS, Unburned AWS, and Unburned–North Camera), which reached peak SWE on 7 May (Figures 2b and 2c, and Table S2 in Supporting Information S1). Probe snow depths collected on 6 May show the north burned transect had accumulated 19 mm (3%) more SWE than the north unburned transect, while south burned aspects had 34 mm (9%) less SWE than unburned south sites (Figures 2b and 2c). Around the time of peak SWE at the Burned–South Camera, the burned south aspect snow survey on 6 April had 9 mm (2%) greater peak SWE than the snow survey near peak SWE on the unburned south aspect (6 May). However, these observed differences in peak SWE were not statistically significant ($p > 0.05$). Between the date of peak SWE on the burned south aspect and peak SWE on all other aspects (15 April—7 May) (yellow period in Figures 2b and 2c), SWE declined at the burned south aspect but continued to increase in the other three burn/aspect locations (Table S2 in Supporting Information S1).

10.1029/2023WR036539

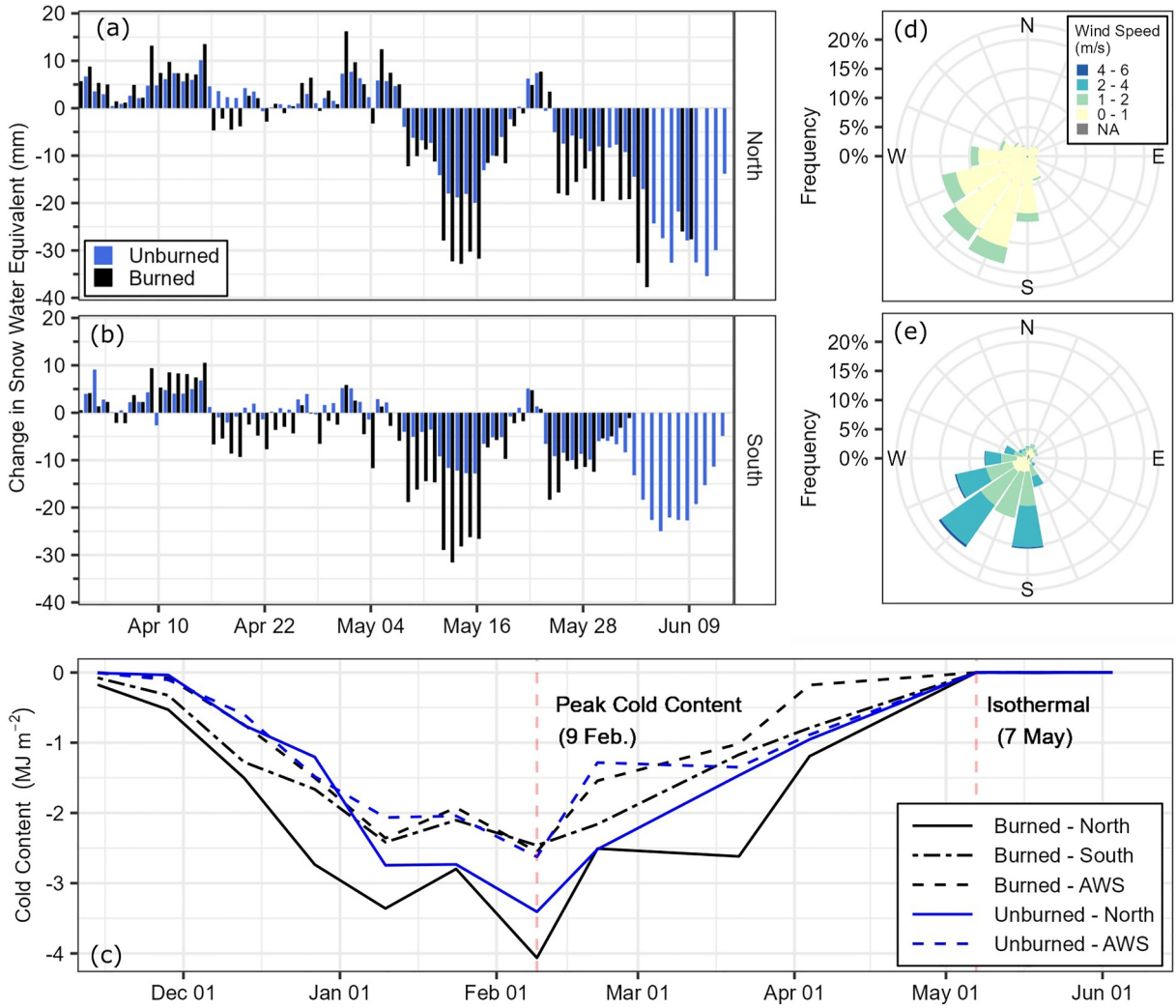

Figure 3. Mean daily change in snow water equivalent (SWE) based on burn condition for (a) north and (b) south aspects. The bars represent the daily change at each of the continuous sites while the horizontal bars show the average daily SWE change between probe surveys. (c) Timeseries of the mean snowpack cold content based on aspect and burn condition. Vertical red lines indicate peak cold content and the survey when all sites are isothermal. Wind rose showing hourly windspeed and direction for each weather station, (d) unburned automated weather station (AWS) and (e) burned AWS.

4.1.2. Melt Patterns

The differences in snowpack properties between the burned and unburned sites were most apparent during the melt period. Between peak SWE (7 May for most burn/aspect categories) and 20 May, when a 5-day storm cycle began which added ~30 cm snow depth, the mean melt rates at the burned north and south sites were 7 and 11 mm d^{-1} greater, respectively, than at the unburned sites (Figures 3a and 3b, and Table S2 in Supporting Information S1). Between probe surveys on 6 May and 19 May, the average daily rate of SWE loss in the burned areas was approximately double that of unburned areas (Figures 3a and 3b, and Table S2 in Supporting Information S1). Following the storm (26 May–3 June), north aspect burned areas continued to melt faster than unburned areas but the difference in melt rates was not as large (Figures 3a and 3b, and Table S2 in Supporting Information S1).

On the probe survey dates of 19 May, 26 May, and 3 June, burned transects held 178, 213, and 244 mm more SWE than unburned transects on north aspects and 192, 231, 186 mm more SWE on south aspects (Figures 2b and 2c). While differences between comparable aspects in the burned and unburned areas were similar during this period, median SWE was substantially less on burned south aspects (0–49 mm) than on burned north aspects (157–316 mm). During the melt period, the IQR expanded on burned north aspects (Figure 2b), with the burned north

IQR growing 246 mm (78%) greater than the IQR on unburned north aspects. Similarly, burned south IQR was 32 mm (29%) greater than comparable unburned areas.

Snow disappearance occurred at the Burned—AWS site on 3 June and at the Burned—North site on 10 June, while all unburned sites became snow free on 14 June (Figures 2b and 2c). The steeply sloped Burned—South site (low northness value) was snow free on 19 May, prior to the 5-day spring snowstorm, and became snow free for the season on 1 June.

4.1.3. Aspect and Burn Condition Influence on Snowpack Cold Content

Snowpack cold content exhibited a distinctive seasonal pattern, with an increase in cold content from November through January, maximum cold content in early February, followed by a decline until all sites were isothermal in early May (Figure 3c). Cold content was greatest on the north burned aspect through 27 December, while the three other sites were similar (Figure 3c). Beginning with the 24 January survey, cold content was more similar between comparable aspects than based on burn/unburned condition, with north aspects having greater cold content than south aspects (Figure 3c). All sites reached a maximum observed cold content during the 9 February survey. Aspect-driven similarities continued until 21 March when snowpack cold content in the burned areas decreased at a greater rate than unburned areas. All sites were isothermal on the 7 May survey (Figure 3c).

4.2. Wind Speed Following Wildfire

Wind speeds at the burned site AWS were generally higher than those at the unburned AWS. Specifically, the burned AWS recorded median seasonal windspeeds of 1.76 m s^{-1} while the wind speeds at the unburned AWS were significantly lower ($p < 0.05$; 0.45 m s^{-1}). At the burned AWS, 40% of all hourly windspeeds were greater than 2 m s^{-1} while there were no occurrences greater than 2 m s^{-1} at the unburned AWS (Figures 3d and 3e). Predominant wind directions were south–southwest at both sites (Figures 3d and 3e).

4.3. Energy Balance Following Wildfire

4.3.1. Snow Surface Albedo

The median broadband albedo at the burned AWS (0.74) was 33% greater than the median unburned albedo (0.53) from 1 December through 28 February (Figure 4a). The median albedo was 22% greater at the burned site (0.69) than the unburned site (0.55) between 1 March and 31 May.

We collected spatially distributed spectral albedo measurements on 15 May (Figures 4c and 4d). We found the spectral albedo in the burned area was 37% less ($p < 0.05$) than the spectral albedo in the unburned areas across all measured wavelengths (350–2500 nm; Figure 4b). In the visible wavelengths (400–700 nm), we found a significant difference ($p < 0.05$) in the median albedos—the burned area albedo (0.44) was 42% lower than the unburned area albedo (0.76). In the 295–2685 nm range, which is captured by the broadband albedo measurements at the AWS, the spectral albedo was 0.24 and 0.37 in the burned and unburned areas, respectively (Figure 4a). Compared to the AWS broadband albedo, these spectral albedo measurements were 23% greater at the unburned site and 36% lower at the burned site.

4.3.2. Shortwave Radiation (K)

Mean daily net shortwave radiation was low during the winter months (1 December −28 February), and gradually increased to maximum values of 133 W m^{-2} (burned) and 59 W m^{-2} (unburned) during the spring (1 March through 31 May; Figure 5a and Table S3 in Supporting Information S1). The burned site received 1.5 and 2.25x (16 and 74 W m^{-2}) more mean net shortwave radiation relative to the unburned site during the winter and spring (Figure 5a and Table S3 in Supporting Information S1). This increase in mean daily net shortwave energy was in part driven by the burned site receiving 2–3x the incoming shortwave radiation of the unburned site (Table S3 in Supporting Information S1). Over the entire study period (1 December–31 May), the burned site received more than double the net shortwave radiation of the unburned site with the difference in cumulative net shortwave between the burned and unburned sites being more than 4x greater in the spring than the winter (Table S3 in Supporting Information S1).

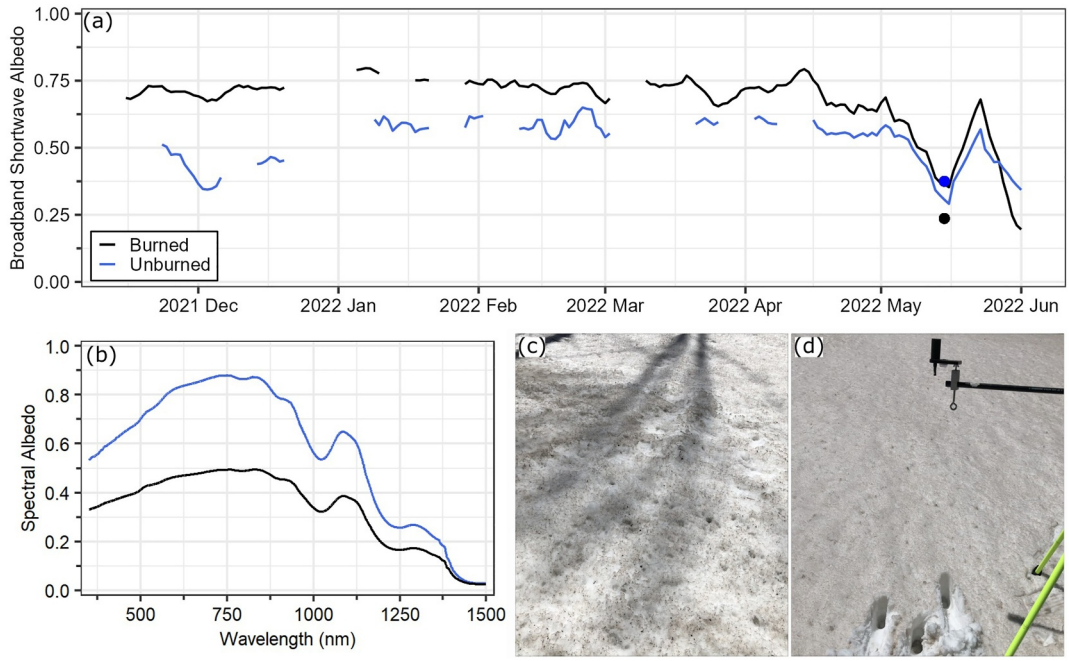

Figure 4. (a) Seven-day running mean of broadband (upward-looking, 385–2,105 nm; downward-looking, 295–2,685 nm) albedo at the burned and unburned automated weather stations. Albedo was calculated as the median value between 1,000 and 1,400 hr on each day. The burned and unburned mean spectral albedo over the 295–2,685 nm is plotted on 15 May as black and blue points. (b) Spectral albedo in burned and unburned locations on 15 May. (c) Snow surface at a burned analytical spectral devices (ASD) measurement location. (d) Unburned snow surface and the ASD remote cosine receptor and tripod. Note: Snow samples were taken after all measurements were collected.

4.3.3. Longwave Radiation (L)

The difference in mean daily net longwave radiation between the sites was more temporally consistent than shortwave radiation, but the burned site was always more negative in magnitude. During the winter and spring, the burned site lost ~30 W m^{-2} more net longwave radiation than the unburned site with minimal seasonal variability (Figure 5b and Table S3 in Supporting Information S1). This difference in net longwave was primarily due to differences in incoming longwave radiation between the sites where the burned site received ~40 W m^{-2} ($p < 0.05$) less incoming longwave energy than the unburned site (Table S3 in Supporting Information S1). Mean daily outgoing radiation declined slightly at the burned sites compared to the unburned sites during the winter and spring but also showed little seasonal variability (Table S3 in Supporting Information S1). These alterations resulted in the burned site losing 2.5 and 3.5*x* more longwave radiation than the unburned site during the winter and spring, respectively (Table S3 in Supporting Information S1).

4.3.4. Net Radiation Flux (R)

The direction of energy flux between the snowpack and atmosphere varied seasonally at both the burned and unburned AWS sites. During the winter, the net radiation flux was negative on approximately 92% of days at the burned AWS and 74% of days at the unburned AWS site (Figure 5c). However, during the spring, net radiation was positive on 76% and 81% of days at the burned and unburned AWS sites, respectively. The magnitude of net radiation flux was primarily a function of burned/unburned condition. Specifically, during the winter, the mean daily net radiation at the burned site was 22 W m^{-2} more negative than the unburned site (Figure 5c and Table S3 in Supporting Information S1). In the spring, the mean daily net radiation at the burned site was 12 W m^{-2} greater than the unburned site (Figure 5c and Table S3 in Supporting Information S1). This seasonality resulted in the burned site losing over 5*x* (~14,600 MJ) more cumulative net radiation than the unburned area during the winter, yet gained nearly double (~9,100 MJ) the cumulative net radiation in the spring (Table S3 in Supporting Information S1).

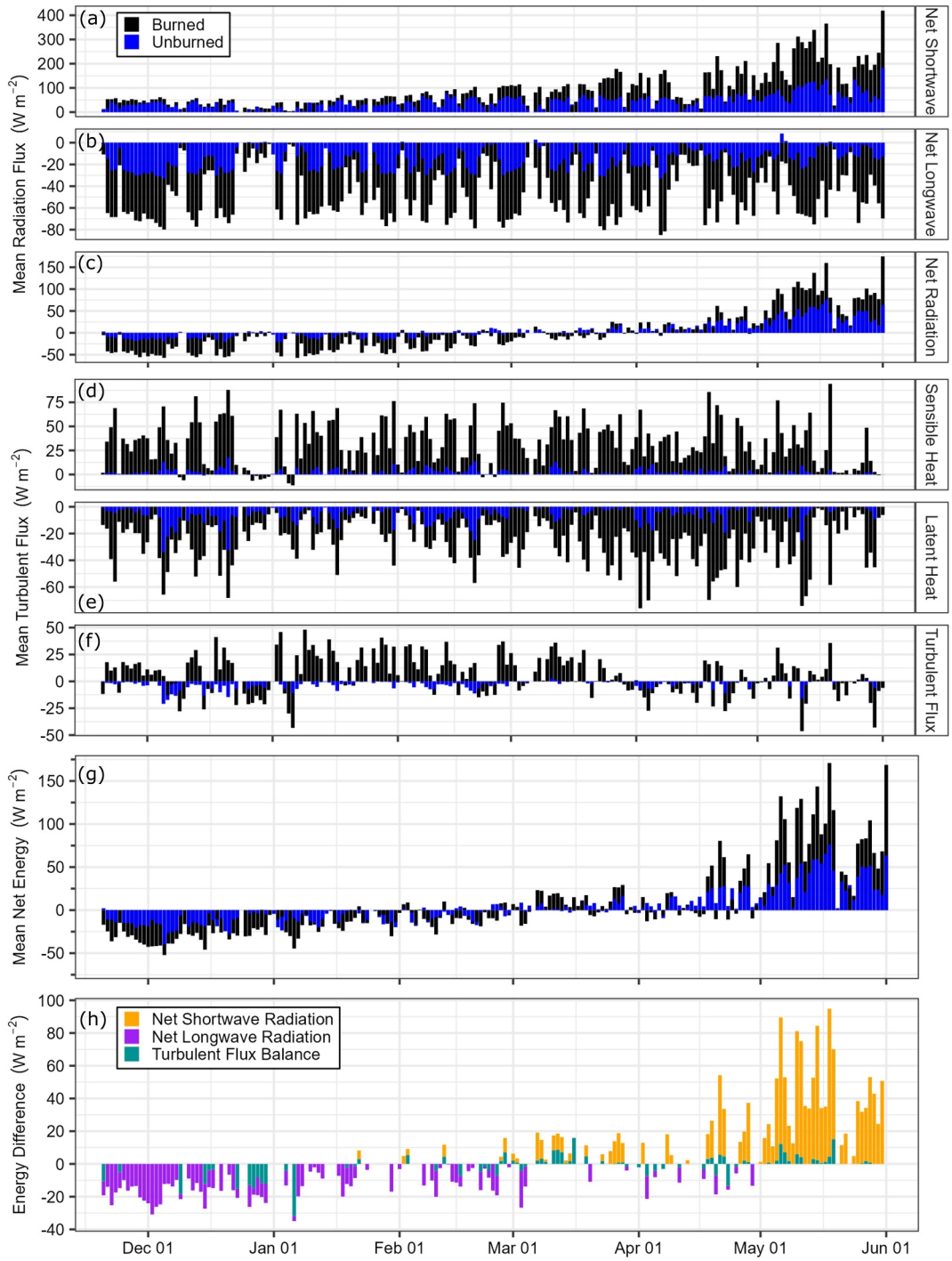

Figure 5. (a) Mean daily net shortwave, (b) longwave, and (c) radiation flux for the burned and unburned automated weather station (AWS) sites. Mean daily (d) sensible, (e) latent, and (f) total turbulent heat fluxes for the burned and unburned AWS sites. (g) Mean daily net energy at the burned and unburned AWS sites. (h) Daily difference between the mean daily net energy at the burned and unburned sites (burned minus unburned), and the proportion of the net difference attributed to each energy balance component.

4.3.5. Turbulent Heat Fluxes (H, L_vE)

Turbulent fluxes were relatively consistent in magnitude throughout the study period at both sites, but were greater in magnitude at the burned site. The average mean daily sensible heat flux at the burned AWS was

29 W m^{-2} greater than the unburned site during the winter and spring (Figure 5d and Table S3 in Supporting Information S1). The mean daily latent heat flux was slightly more seasonally dependent, the burned site lost 16 and 26 W m^{-2} more latent heat than the unburned site in the winter and spring, respectively (Figure 5e and Table S3 in Supporting Information S1). This increase in latent heat flux indicates a greater potential for sublimation at the burned site throughout the winter. The mean daily net turbulent flux caused a net energy gain at the burned sites during both seasons, however the difference in net turbulent flux between the burned and unburned sites was greater in the winter (14 W m^{-2}) than the spring (2 W m^{-2}) (Figure 5f and Table S3 in Supporting Information S1).

Both sensible and latent heat fluxes varied considerably during different weather conditions, with the lowest magnitude sensible and latent heat fluxes during periods of snowfall and the greatest values during dry periods. During both the winter and spring, sensible heat flux added a cumulative total of ∼20,000 MJ (10–15x) more energy at the burned site than the unburned site with little seasonal variability (Table S3 in Supporting Information S1). However, the cumulative latent heat flux was a greater loss at the burned site during both the winter and spring (Table S3 in Supporting Information S1). At the burned site, the sensible heat increases caused the cumulative net turbulent flux balance to be positive (snowpack gained energy), yet at the unburned sites the cumulative turbulent flux was negative (snowpack lost energy) during both seasons (Table S3 in Supporting Information S1).

4.3.6. Daily Net Energy (Q)

The mean daily net energy at both the burned and unburned sites was consistently negative (90% of days at the burned; 89% unburned) during the winter (1 December–28 February). During this time, the mean daily net energy loss at the burned site was 8 W m^{-2} greater than at the unburned site (Figure 5g and Table S3 in Supporting Information S1). This difference in the energy balance resulted in the burned site losing approximately double (∼6,000 MJ) the cumulative daily net energy during the winter than the unburned site (Table S3 in Supporting Information S1). The energy balance flipped during the spring (1 March–31 May), with the burned site receiving 15 W m^{-2} greater mean daily net energy and double (∼10,500 MJ) the cumulative net energy than the unburned site (Figure 5g and Table S3 in Supporting Information S1).

Before 1 March, the differences in net energy between burned and unburned areas were primarily due to changes in the net longwave and turbulent flux components of the energy balance, which created a more negative the energy balance in the burned area compared to the unburned area (Figure 5h). The primary component of the difference between the burned and unburned sites then became the net shortwave radiation through the spring, with some positive turbulent flux differences, causing the net energy at the burned site to become more positive than at the unburned site (Figure 5h).

5. Discussion

Wildfire fundamentally alters the forest environment, leading to key changes in the snowpack energy balance and snowpack characteristics (e.g., melt rates). We highlight specific connections between the altered energy balance and changes to snowpack characteristics in Figure 6, which provides a framework for the discussion.

5.1. Influences of Burn Condition and Aspect

The greatest difference in SWE accumulation and melt rates occurred based on aspect regardless of the burn condition. This finding matches the previous literature in burned and unburned forests that illustrates the variability in SWE accumulation and ablation patterns based on aspect and burn severity (Anderson et al., 2014; Maxwell et al., 2019; Moeser et al., 2020). We found no difference in peak SWE magnitude between our probe snow surveys in burned and unburned areas (Figures 6a and 6b). Previous western U.S. studies have reported decreases of 10%–50% (Giovando & Niemann, 2022; Harpold et al., 2014; Smoot & Gleason, 2021) and increases of 11% (Gleason & Nolin, 2016) in peak SWE post-fire with drivers of differences being eco-region and snow regime. There are multiple competing factors that can influence peak SWE post-fire, including increased accumulation due to reduced canopy interception, increased snowpack declines due to greater sublimation, enhanced wind transport, and earlier melt that offsets late season accumulation gains (Figures 6a and 6b). Harpold et al. (2014) observed greater accumulation in burned areas relative to unburned areas on a per storm basis but found lower peak SWE on the season. The reason for this per storm versus seasonal discrepancy was attributed to

10.1029/2023WR036539

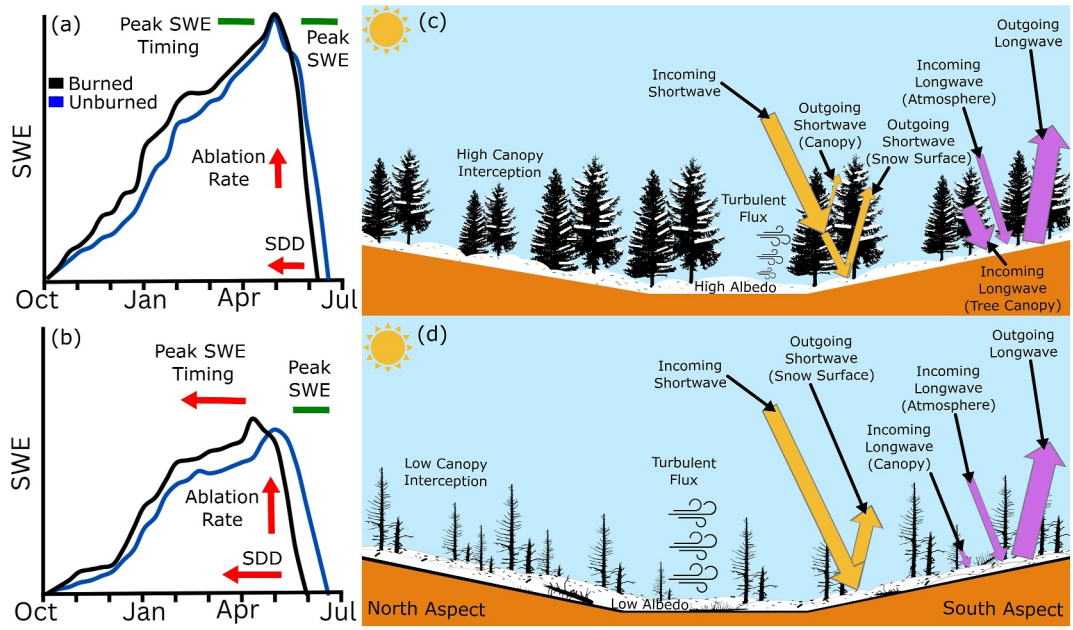

Figure 6. Changes in the snowpack characteristics on (a) north and (b) south burned aspects where blue indicates unburned areas, black is burned areas, arrow size indicates the magnitude of the change following wildfire, and horizontal bars indicate no significant difference between the unburned and burned areas. Snowpack energy balance for a clear-sky, daytime condition (c) without wildfire and (d) following wildfire based on aspect where arrow and icon size represents relative change.

enhanced sublimation in burned areas. Similarly, the increased latent heat fluxes at our burned site indicates greater sublimation relative to unburned areas (Lundquist et al., 2024). For example, in late March and early April, we observed SWE declines on both burned aspects (Figures 2b and 2c) at a time when the snowpack still had considerable cold content (Figure 3c). During this period, the latent heat losses at the burned site were significantly greater than at the unburned site (Figure 5e). Later in the season, the role of earlier melt in decreased peak SWE magnitudes was evident. The burned south site reached peak SWE 22 days earlier than other sites because late season SWE gains were offset by intermittent SWE losses, which did not occur at the other sites.

Our finding of no peak SWE difference between the burned and unburned areas differs from 2020 to 2021 winter observations within the same study area where peak SWE was 17%–25% less in burned sites relative to unburned sites (Kampf et al., 2022; McGrath et al., 2023). The discrepancies in peak SWE between the 2020 and 2021 and 2021–2022 winters within the study area could represent sensitivity to interannual snow accumulation patterns. Although both winters were average when compared to the 30-year median, snow accumulated frequently during the 2020–2021 winter, while the 2021–2022 winter was characterized by long dry periods punctuated by short periods of rapid snow accumulation. Additionally, the use of more automated sites and more extensive probe transects during the 2021–2022 winter could have contributed to the observed differences.

At the burned south site, peak SWE occurred 22 days earlier than the unburned south site while this date was the same for burned/unburned north aspects (Figures 6a and 6b). These results highlight the important, but nuanced, role of aspect on the timing of peak SWE since the changes are outside the average 6–10 days range reported in previous literature for the western U.S (Giovando & Niemann, 2022; Smoot & Gleason, 2021). One possible explanation for the difference on south aspects is that previous studies examined SNOTEL sites which are typically in open meadows with low surface slopes, while our sites have slopes between 2 and 24°.

Following peak SWE, melt rates increased in the burned areas on both north and south slopes, with the greatest increases on burned south aspects (Figures 6a and 6b). The increased average daily probe-derived melt rates in the burned areas prior to the late-May snowstorm caused earlier snow disappearance in the burned area on all aspects

(Figures 6a and 6b). In contrast to the differences in peak SWE between the 2020 and 2021 and 2021–2022 winters in this study area, the change in SDD between burned and unburned areas was consistent between the years (11–13 days) (McGrath et al., 2023), and were similar to the average for the Southern Rockies (11.7 days) (Giovando & Niemann, 2022), but are less than the 23 days reported by Gleason et al. (2013) from the High Cascades. This difference in SDD between eco-regions highlights the complexity of the post-wildfire response in different environments and the need for further studies in a variety of eco-regions and snow regimes. Post-fire response variability has direct implications for water resources and ecosystem recovery. For example, in the Southern Rockies, the earlier snow free date in the burned areas, particularly on burned south aspects, could hamper revegetation due to the earlier onset of evapotranspiration from the soil, exacerbating the water limited growing regime and slowing forest recovery (Stevens-Rumann & Morgan, 2019; Webb et al., 2023).

Our primary focus has been on quantifying energy balance differences in the spring, as these differences led to increased melt rates and earlier snow disappearance in the burned areas. However, these energy balance differences are also present in the fall and can lead to variations in early season snow persistence that influence spatial patterns later in the season. Our observations showed that north burned aspects held consistently greater snow depths throughout the entire study period. This difference can be attributed, in part, to accumulation from an early October snowstorm that persisted on burned north aspects but completely melted from burned south aspects (Figure S4 in Supporting Information S1). In unburned areas, the presence of forest canopy made observations inconclusive, but it appeared that steep south-facing unburned slopes had melted completely, while all other unburned slopes retained snow. While we do not know the depth of snow that remained prior to the start of our regular surveys, we attribute the relatively consistent difference in snow depth identified throughout the accumulation period to aspect-dependent energy balance differences following this early season snowfall. A portion of this difference may also be attributed to site-specific preferential wind deposition of snow on our north burned aspects, which was observed during the periodic site visits.

5.2. Snowpack Energy Balance

Our study found significant changes to all components of the surface energy balance at the burned site relevant to the unburned site. The driver of the difference in daily mean net energy varied seasonally: during the winter, greater net longwave radiation losses led to a substantially more negative energy balance at the burned site, while in the spring, substantial increases in net shortwave radiation led to a much more positive net energy balance at the burned site (Figures 6b and 6c, and Table S3 in Supporting Information S1). Importantly, changes in turbulent fluxes were not negligible, as the burned site consistently gained energy from the net turbulent flux, while the unburned site experienced more losses in energy from turbulent fluxes.

5.2.1. Increased Net Shortwave Radiation

The loss of forest canopy in wildfires increases shortwave radiation that reaches the snow surface, while remaining trunks are persistent sources of soot/ash that lead to reductions in snow albedo. Collectively, these changes fundamentally alter the shortwave radiation balance of post-fire snow environments. Within this framework, one surprising aspect of our AWS observations was the consistently lower albedo at the unburned site, particularly during the accumulation season, relative to the burned site. Given the densely forested conditions of the unburned site, we attribute this observation to three factors: (a) shadows on the snow surface while the sensor had direct or nearly direct illumination (Figure S1e in Supporting Information S1), (b) the accumulation of leaf litter on the snow surface at the unburned site (Figure S5 in Supporting Information S1), and (c) a sensor footprint that integrated both snow and trees at the unburned site given the close (~3 m) proximity of trees, essentially yielding a land surface albedo measurement rather than a pure snow surface albedo measurement (Figure S1 in Supporting Information S1).

During the melt season, the burned site had a slightly lower minimum albedo relative to the unburned site but unlike previous studies (e.g., 40% and 60% decreases identified by Gleason and Nolin (2016) and Hatchett et al. (2023) during melt), our stations did not document a comparable precipitous decline in snow albedo. Potential explanations for this difference include (a) a widespread dust on snow event in mid-April that uniformly decreased the albedo across the entire study site and therefore reduced the preferential burn area albedo decline relative to clean snow (Rittger, 2022), and (b) a late-season snowstorm that increased the albedo across

all sites for a ∼5-day period in late May, which are a common occurrence for this eco-region (e.g., McGrath et al., 2023).

At the peak of the snowmelt season (15 May), our distributed spectroradiometer observations (which included open unburned sites) revealed differences between burned and unburned conditions that are more closely aligned with previous work (e.g. (Gleason et al., 2013),). Visible wavelength albedo at the burned sites were 42% less than comparable unburned areas (Figures 6b and 6c), which is comparable to previous studies, including the 40% decline found during prior winter (the first post-fire) using similar methods (McGrath et al., 2023). These distributed observations are contrasted with the station point observations, as the burned station albedo was 18% greater than the unburned site on this date.

Although our station data did not show a consistent decline in snow albedo relative to the unburned site, the loss of canopy in the burned area, coupled with a low albedo during the melt period, led to a more than doubling of cumulative net shortwave energy. This considerable increase in net shortwave energy highlights the transformative and long-lasting role that fires can have on the snowpack energy balance. It also highlights a need to better understand the relative contribution of albedo decline and increased incoming shortwave radiation, as the recovery timelines for albedo and forest canopy are significantly different. Using our paired energy balance observations and spectroradiometer albedo values, we found that the increase in downwelling shortwave radiation in the spring (1 March—31 May) was 6*x* more impactful than the change in albedo if wildfire had not occurred (Table S4 in Supporting Information S1). Using melt season albedo values reported in McGrath et al. (2023) and Gleason et al. (2013), we found comparable results: the increase in net shortwave radiation due to canopy loss was 5–6*x* greater than the decreased albedo in the burned areas (Table S4 in Supporting Information S1). This highlights key differences in the longevity of wildfire impacts on snowpack characteristics: post-fire black carbon radiative forcing declines exponentially in the first 5 years post-fire (e.g., Gleason et al., 2019) while forest canopy can take more than a decade to recover (e.g., Bright et al., 2019), if it does at all given current climate conditions (e.g., Stevens-Rumann & Morgan, 2019). Importantly, however, this post-fire response will vary considerably between eco-regions given differences in the partitioning of energy balance components, snowpack characteristics (e.g., peak SWE magnitude and timing), snowfall frequency during the melt season, as well as wildfire and forest characteristics (e.g., tree size, spacing, species, mortality %, etc.). Consequently, the results presented here, and in other site-specific studies, need to be evaluated in the context of these characteristics before being applied to other burned locations.

5.2.2. Altered Longwave Radiation, Turbulent Fluxes, and Net Energy

Unlike net shortwave radiation, the net longwave radiation difference between the burned and unburned sites was consistent between 1 December and 31 May, which is attributed to the loss of tree biomass at the burned site (Figures 6c and 6d). Trees absorb shortwave radiation and re-emit longwave radiation (Rouse, 1984), so the loss of canopy greatly reduced incoming longwave radiation and shifted net longwave markedly more negative at the burned site. We have observed consistent melt-out patterns in the burned site during the first three winters post-fire, where snow first disappears in the immediate vicinity of the remaining trunks before expanding radially (Figure S1 in Supporting Information S1). While this pattern could be the result of lower snow accumulation or a more positive shortwave balance due to a lower albedo, we hypothesize that the remaining trunks remain a major longwave energy source. Trunks modify the energy balance in their immediate (10s of cm) vicinity and is not being accurately captured by our existing station network (i.e., few burned trees are within the footprint for the net radiometers). However, given the cumulative area of these trunks, this is likely an important component of the energy balance at the landscape-scale.

The seasonality of net shortwave radiation resulted in the net radiation switching from considerably negative (due to longwave losses) to close to zero in early March (due to shortwave gains; Figure 5c) at both burned and unburned locations. While the net radiation stayed around zero until late March (Figure 5c), the net energy become consistently positive in early March (Figure 5g). During most of March, the net turbulent flux was consistently positive (Figure 5f) at the burned site. While the seasonally increasing net shortwave brought the net radiation close to zero, it was the positive turbulent flux during March that caused the net energy to switch from constantly negative to consistently positive in early March indicating that the magnitude of sensible heat was greater than the magnitude of latent heat (Figure 5h). As the amount of incoming net shortwave continued to

increase through the spring, the importance of the net shortwave in the difference between the burned and unburned areas became greater (Figure 5h). This earlier net energy balance increase again emphasizes the importance of the loss of canopy on burned area snowpack energy balances in the Southern Rockies due to the increased incoming shortwave radiation and wind speeds, ultimately driving greater net shortwave radiation and turbulent fluxes.

5.2.3. Net Energy Influence on Cold Content

From mid-December until mid-January, the snowpack mass increased at its highest rate (200–300 mm/month) of the entire season. This increase in mass coincided with the highest rate of cold content development across all four aspect and burn categories, in line with the findings of Jennings et al. (2018). Cold content continued to increase through the early February surveys, coinciding with lower rates of mass gain and negative net energy balances. However, in mid-February the cold content at all sites began to decline, despite an increasing snowpack mass, suggesting that this decrease in cold content was caused by snowpack energy gains. This observation is surprising, as the station-calculated net energy balance remained negative until early March (Figures 3c and 5g). To further explore this result, we compared the change in cold content and cumulative net energy between each of the snow pit measurement dates (Figure S6 in Supporting Information S1). This analysis identified two periods at the burned site between late January and mid-February that the change in cold content decreased (snowpack warmed or lost mass) but cumulative net energy was negative, a physically unrealistic scenario. During both periods (10 January–24 January and 9 February–21 February) (Figure S6 in Supporting Information S1), our observations indicate that minimal accumulation occurred and density remained constant. Assessing whether this discrepancy persists over multiple years and sites is warranted, but also highlights potential shortcomings in our ability to accurately measure all aspects of the snowpack energy balance. Improvements could be made by: (a) directly measuring turbulent fluxes, (b) more frequent and a greater number of snow pits to quantify cold content, (c) continuous measurements of snow surface temperature, snowpack temperatures, and ground heat flux.

6. Conclusions

Our research shows that complex terrain modulates post-wildfire snowpack impacts. We found no difference in probe-derived peak SWE between burned and unburned areas for both north and south aspects. However, south-facing burned slopes reached peak SWE 22 days before all other aspects and became snow free up to 11 days earlier than other aspects and burn conditions. Melt rates were dependent on the burn condition with burned areas melting up to twice as fast as unburned areas on both north and south aspects. All components of the surface energy balance were altered at the burned site relative to the unburned site. The burned site lost 12 W m^{-2} more daily net energy in the winter (1 December–28 February) than at the unburned site due to greater net longwave losses from the loss of forest biomass at the site. However, during the spring (1 March–31 May) the loss of canopy allowed ∼3*x* more incoming shortwave energy to impact the snow surface and the albedo was 37% lower, resulting in 12 W m^{-2} more daily net energy at the burned site than the unburned site. The increase in incoming shortwave radiation resulted in 6*x* more net shortwave energy gain than the decrease in snow albedo.

Incorporating aspect-based analysis of SWE accumulation and melt following wildfire and paired energy balance analysis between burned and unburned areas furthers our understanding of how wildfire alters the physical processes within high-elevation seasonal snowpacks. Additionally, we also gained knowledge on how the changes observed in snowpack accumulation and ablation patterns are explained by the alterations of the net energy within burned areas. Using this work, operational and scientific modeling of runoff timing and magnitude can be improved, providing essential information to water managers and decision makers in the wake of increased high-elevation wildfires (Alizadeh et al., 2021; Iglesias et al., 2022; Kampf et al., 2022). By analyzing the alteration of the mass and energy balances following wildfire across complex terrain within a high-elevation continental snow zone, our research provides a nuanced assessment of how wildfire impacted snowpack accumulation and melt, which can help inform decision making for water resource and snowmelt flood risk management.

Data Availability Statement

The automated weather station, time lapse camera snow depths, and snow pit and snow probe data used for the mass and energy balance analysis along with the turbulent flux modeling code used in the study are available on HydroShare (Reis & McGrath, 2024).

Acknowledgments
This research was funded in part by The Geological Society of America Research Grant, the Colorado State University Evelyn I. Clark and Warner College of Natural Resources Scholarships, the Sigma Xi Research Grant, and the Colorado Mountain Club Foundation Research Grant. We thank Huihui Zhang and Kevin Yemoto with the USDA ARS in Fort Collins, CO for supporting the spectroradiometer observations. Thank you to Amber Scott, John Kemper, Lucas Zeller, Megan Sears, Aly Cheney, Anna Marshall, Holly Proulx, Tara Vessella, and Lucas Dolliver for their field assistance. Thank you to Adrian Harpold and an anonymous reviewer for their thoughtful comments that helped improve the clarity of our findings. Any use of trade, firm, or product names is for descriptive purposes only and does not imply endorsement by the U.S. Government.

References

Alizadeh, M. R., Abatzoglou, J. T., Luce, C. H., Adamowski, J. F., Farid, A., & Sadegh, M. (2021). Warming enabled upslope advance in Western US forest fires. *Proceedings of the National Academy of Sciences of the United States of America*, *118*(22), e2009717118. https://doi.org/10.1073/pnas.2009717118

Anderson, B. T., McNamara, J. P., Marshall, H.-P., & Flores, A. N. (2014). Insights into the physical processes controlling correlations between snow distribution and terrain properties. *Water Resources Research*, *50*(6), 4545–4563. https://doi.org/10.1002/2013WR013714

Andreas, E. L. (2002). Parameterizing scalar transfer over snow and ice: A review. *Journal of Hydrometeorology*, *3*(4), 417–432. https://doi.org/10.1175/1525-7541(2002)003<0417:PSTOSA>2.0.CO;2

Bales, R. C., Molotch, N. P., Painter, T. H., Dettinger, M. D., Rice, R., & Dozier, J. (2006). Mountain hydrology of the Western United States. *Water Resources Research*, *42*(8), W08432. https://doi.org/10.1029/2005WR004387

Barnett, T. P., Adam, J. C., & Lettenmaier, D. P. (2005). Potential impacts of a warming climate on water availability in snow-dominated regions. *Nature*, *438*(7066), 303–309. https://doi.org/10.1038/nature04141

Barnhart, T. B., Molotch, N. P., Livneh, B., Harpold, A. A., Knowles, J. F., & Schneider, D. (2016). Snowmelt rate dictates streamflow. *Geophysical Research Letters*, *43*(15), 8006–8016. https://doi.org/10.1002/2016GL069690

Boon, S. (2009). Snow ablation energy balance in a dead forest stand. *Hydrological Processes*, *23*(18), 2600–2610. https://doi.org/10.1002/hyp.7246

Bright, B. C., Hudak, A. T., Kennedy, R. E., Braaten, J. D., & Henareh Khalyani, A. (2019). Examining post-fire vegetation recovery with Landsat time series analysis in three Western North American forest types. *Fire Ecology*, *15*(1), 8. https://doi.org/10.1186/s42408-018-0021-9

Brutsaert, W. (1982). *Evaporation into the atmosphere*. Springer Netherlands. https://doi.org/10.1007/978-94-017-1497-6

Burles, K., & Boon, S. (2011). Snowmelt energy balance in a burned forest plot, Crowsnest Pass, Alberta, Canada. *Hydrological Processes*, *25*(19), 3012–3029. https://doi.org/10.1002/hyp.8067

Cayan, D. R., Dettinger, M. D., Kammerdiener, S. A., Caprio, J. M., & Peterson, D. H. (2001). Changes in the onset of spring in the western United States. *Bulletin of the American Meteorological Society*, *82*(3), 399–415. https://doi.org/10.1175/1520-0477(2001)082<0399:CITOOS>2.3.CO;2

Clow, D. W. (2010). Changes in the timing of snowmelt and streamflow in Colorado: A response to recent warming. *Journal of Climate*, *23*(9), 2293–2306. https://doi.org/10.1175/2009JCLI2951.1

Dudley, R. W., Hodgkins, G. A., McHale, M. R., Kolian, M. J., & Renard, B. (2017). Trends in snowmelt-related streamflow timing in the conterminous United States. *Journal of Hydrology*, *547*, 208–221. https://doi.org/10.1016/j.jhydrol.2017.01.051

Elder, K., Dozier, J., & Michaelsen, J. (1989). Spatial and temporal variation of net snow accumulation in a small alpine watershed, Emerald Lake Basin, Sierra Nevada, California, U.S.A. *Annals of Glaciology*, *13*, 56–63. https://doi.org/10.3189/s0260305500007643

Elder, K., Dozier, J., & Michaelsen, J. (1991). Snow accumulation and distribution in an alpine watershed. *Water Resources Research*, *27*(7), 1541–1552. https://doi.org/10.1029/91WR00506

Giovando, J., & Niemann, J. D. (2022). Wildfire impacts on snowpack phenology in a changing climate within the Western U.S. *Water Resources Research*, *58*(8), e2021WR031569. https://doi.org/10.1029/2021WR031569

Gleason, K. E., McConnell, J. R., Arienzo, M. M., Chellman, N., & Calvin, W. M. (2019). Four-fold increase in solar forcing on snow in Western U.S. burned forests since 1999. In *Nature communications*, (Vol. 10). 2026, Springer Science and Business Media LLC. https://doi.org/10.1038/s41467-019-09935-y

Gleason, K. E., & Nolin, A. W. (2016). Charred forests accelerate snow albedo decay: Parameterizing the post-fire radiative forcing on snow for three years following fire. *Hydrological Processes*, *30*(21), 3855–3870. https://doi.org/10.1002/hyp.10897

Gleason, K. E., Nolin, A. W., & Roth, T. R. (2013). Charred forests increase snowmelt: Effects of burned woody debris and incoming solar radiation on snow ablation. *Geophysical Research Letters*, *40*(17), 4654–4661. https://doi.org/10.1002/grl.50896

Goeking, S. A., & Tarboton, D. G. (2020). Forests and water yield: A synthesis of disturbance effects on streamflow and snowpack in Western coniferous forests. *Journal of Forestry*, *118*(2), 172–192. https://doi.org/10.1093/jofore/fvz069

Goeking, S. A., & Tarboton, D. G. (2022). Variable streamflow response to forest disturbance in the Western US: A large-sample hydrology approach. *Water Resources Research*, *58*(6), e2021WR031575. https://doi.org/10.1029/2021WR031575

Hale, K. E., Jennings, K. S., Musselman, K. N., Livneh, B., & Molotch, N. P. (2023). Recent decreases in snow water storage in Western North America. *Communications Earth & Environment*, *4*(1), 170. https://doi.org/10.1038/s43247-023-00751-3

Hall, D. K., Crawford, C. J., DiGirolamo, N. E., Riggs, G. A., & Foster, J. L. (2015). Detection of earlier snowmelt in the wind river range, Wyoming, using Landsat imagery, 1972–2013. *Remote Sensing of Environment*, *162*, 45–54. https://doi.org/10.1016/j.rse.2015.01.032

Hammond, J. C., Sexstone, G. A., Putman, A. L., Barnhart, T. B., Rey, D. M., Driscoll, J. M., et al. (2023). High resolution SnowModel simulations reveal future elevation-dependent snow loss and earlier, flashier surface water input for the Upper Colorado River Basin. *Earth's Future*, *11*(2), e2022EF003092. https://doi.org/10.1029/2022EF003092

Hardy, J. P., Davis, R. E., Jordan, R., Li, X., Woodcock, C., Ni, W., & McKenzie, J. C. (1997). Snow ablation modeling at the stand scale in a boreal jack pine forest. *Journal of Geophysical Research*, *102*(24), 29397–29405. https://doi.org/10.1029/96jd03096

Harpold, A. A., Guo, Q., Molotch, N., Brooks, P. D., Bales, R., Fernandez-Diaz, J. C., et al. (2014). LiDAR-derived snowpack data sets from mixed conifer forests across the Western United States. *Water Resources Research*, *50*(3), 2749–2755. https://doi.org/10.1002/2013WR013935

Hatchett, B. J., Koshkin, A. L., Guirguis, K., Rittger, K., Nolin, A. W., Heggli, A., et al. (2023). Midwinterdry spells amplify post-fire snowpackdecline. *Geophysical Research Letters*, *50*(3), e2022GL101235. https://doi.org/10.1029/2022GL101235

Iglesias, V., Stavros, N., Balch, J. K., Barrett, K., Cobian-Iñiguez, J., Hester, C., et al. (2022). Fires that matter: Reconceptualizing fire risk to include interactions between humans and the natural environment. *Environmental Research Letters*, *17*(4), 045014. https://doi.org/10.1088/1748-9326/AC5C0C

Jennings, K. S., Kittel, T. G. F., & Molotch, N. P. (2018). Observations and simulations of the seasonal evolution of snowpack cold content and its relation to snowmelt and the snowpack energy budget. In *The cryosphere*, (Vol. 12(5), pp. 1595–1614). Copernicus GmbH. https://doi.org/10.5194/tc-12-1595-2018

Kampf, S. K., Mcgrath, D., Sears, M. G., Fassnacht, S. R., Kiewiet, L., & Hammond, J. C. (2022). Increasing wildfire impacts on snowpack in the Western U.S. *Proceedings of the National Academy of Sciences*, *119*(39), e2200333119. https://doi.org/10.1073/pnas.2200333119

Li, D., Wrzesien, M. L., Durand, M., Adam, J., & Lettenmaier, D. P. (2017). How much runoff originates as snow in the Western United States, and how will that change in the future? *Geophysical Research Letters*, *44*(12), 6163–6172. https://doi.org/10.1002/2017GL073551

Liston, G. E., Haehnel, R. B., Sturm, M., Hiemstra, C. A., Berezovskaya, S., & Tabler, R. D. (2007). Simulating complex snow distributions in windy environments using SnowTran-3D. *Journal of Glaciology*, *53*(181), 241–256. https://doi.org/10.3189/172756507782202865

Loiselle, D., Du, X., Alessi, D. S., Bladon, K. D., & Faramarzi, M. (2020). Projecting impacts of wildfire and climate change on streamflow, sediment, and organic carbon yields in a forested watershed. *Journal of Hydrology*, *590*, 125403. https://doi.org/10.1016/j.jhydrol.2020.125403

Lundquist, J. D., Vano, J., Gutmann, E., Hogan, D., Schwat, E., Haugeneder, M., et al. (2024). Sublimation of Snow. *Bulletin of the American Meteorological Society*, *105*(6), E975–E990. https://doi.org/10.1175/BAMS-D-23-0191.1

Maina, F. Z., & Siirila-Woodburn, E. R. (2020). Watersheds dynamics following wildfires: Nonlinear feedbacks and implications on hydrologic responses. *Hydrological Processes*, *34*(1), 33–50. https://doi.org/10.1002/hyp.13568

Mandal, A., Angchuk, T., Azam, M. F., Ramanathan, A., Wagnon, P., Soheb, M., & Singh, C. (2022). An 11-year record of wintertime snow-surface energy balance and sublimation at 4863ma.s.l. On the Chhota Shigri Glacier moraine (western Himalaya, India). *The Cryosphere*, *16*(9), 3775–3799. https://doi.org/10.5194/tc-16-3775-2022

Maxwell, J. D., Call, A., & Clair, S. B. S. (2019). Wildfire and topography impacts on snow accumulation and retention in montane forests. *Forest Ecology and Management*, *432*(2018), 256–263. https://doi.org/10.1016/j.foreco.2018.09.021

McCabe, G. J., & Clark, M. P. (2005). Trends and variability in snowmelt runoff in the Western United States. *Journal of Hydrometeorology*, *6*(4), 476–482. https://doi.org/10.1175/JHM428.1

McGrath, D., Zeller, L., Bonnell, R., Reis, W., Kampf, S., Williams, K., et al. (2023). Declines in Peak Snow Water Equivalent and Elevated Snowmelt Rates Following the 2020 Cameron Peak Wildfire in Northern Colorado. *Geophysical Research Letters*, *50*(6), e2022GL101294. https://doi.org/10.1029/2022GL101294

Moeser, C. D., Broxton, P. D., Harpold, A., & Robertson, A. (2020). Estimating the effects of forest structure changes from wildfire on snow water resources under varying meteorological conditions. *Water Resources Research*, *56*(11), 1–23. https://doi.org/10.1029/2020WR027071

Molotch, N. P., Brooks, P. D., Burns, S. P., Litvak, M., Monson, R. K., McConnell, J. R., & Musselman, K. (2009). Ecohydrological controls on snowmelt partitioning in mixed-conifer sub-alpine forests. *Ecohydrology*, *2*(2), 129–142. https://doi.org/10.1002/eco.48

Molotch, N. P., Colee, M. T., Bales, R. C., & Dozier, J. (2005). Estimating the spatial distribution of snow water equivalent in an alpine basin using binary regression tree models: The impact of digital elevation data and independent variable selection. *Hydrological Processes*, *19*(7), 1459–1479. https://doi.org/10.1002/hyp.5586

Moore, C., Kampf, S., Stone, B., & Richer, E. (2015). A GIS-based method for defining snow zones: Application to the Western United States. *Geocarto International*, *30*(1), 62–81. https://doi.org/10.1080/10106049.2014.885089

Mote, P. W., Hamlet, A. F., Clark, M. P., & Lettenmaier, D. P. (2005). Declining mountain snowpack in Western North America. *Bulletin of the American Meteorological Society*, *86*(1), 39–50. https://doi.org/10.1175/BAMS-86-1-39

Mote, P. W., Li, S., Lettenmaier, D. P., Xiao, M., & Engel, R. (2018). Dramatic declines in snowpack in the Western US. *Npj Climate and Atmospheric Science*, *1*(1), 2. https://doi.org/10.1038/s41612-018-0012-1

Mueller, S. E., Thode, A. E., Margolis, E. Q., Yocom, L. L., Young, J. D., & Iniguez, J. M. (2020). Climate relationships with increasing wildfire in the southwestern US from 1984 to 2015. *Forest Ecology and Management*, *460*, 117861. https://doi.org/10.1016/J.FORECO.2019.117861

Murray, F. W. (1967). On the Computation of Saturation Vapor Pressure. *Journal of Applied Meteorology*, *6*(1), 203–204. https://doi.org/10.1175/1520-0450(1967)006<0203:OTCOSV>2.0.CO;2

Musselman, K. N., Clark, M. P., Liu, C., Ikeda, K., & Rasmussen, R. (2017). Slower snowmelt in a warmer world. *Nature Climate Change*, *7*(3), 214–219. https://doi.org/10.1038/nclimate3225

O'Leary, D., III, Hall, D. K., Medler, M., Matthews, R., & Flower, A. (2019). Snowmelt Timing Maps Derived from MODIS for North America, Version 2, 2001–2018 [Dataset]. *Oak Ridge, Tennessee: ORNL DAAC*. https://doi.org/10.3334/ORNLDAAC/1712

Reis, W., & McGrath, D. (2024). Data for Quantifying aspect-dependent snowpack response to high-elevation wildfire in the southern rocky mountains [Dataset]. *HydroShare*. Retrieved from https://www.hydroshare.org/resource/868df9f8bdac495e876fb36220eb0f9d

Rittger, K. (2022). The West's tale of two seasons. Retrieved from https://nsidc.org/snow-today/monthly-insights/wests-tale-two-seasons

Roth, T. R., & Nolin, A. W. (2017). Forest impacts on snow accumulation and ablation across an elevation gradient in a temperate montane environment. *Hydrology and Earth System Sciences*, *21*(11), 5427–5442. https://doi.org/10.5194/hess-21-5427-2017

Rouse, W. R. (1984). Microclimate at Arctic Tree Line 1. Radiation Balance of Tundra and Forest. In *Water resources research*, (Vol. 20(1), pp. 57–66). American Geophysical Union (AGU). https://doi.org/10.1029/wr020i001p00057

Shi, K., & Touge, Y. (2023). Identifying the shift in global wildfire weather conditions over the past four decades: An analysis based on change-points and long-term trends. *Geoscience Letters*, *10*(1), 3. https://doi.org/10.1186/s40562-022-00255-6

Smoot, E. E., & Gleason, K. E. (2021). Forest Fires Reduce Snow-Water Storage and Advance the Timing of Snowmelt across the Western U.S. *Water*, *13*(24), 3533. https://doi.org/10.3390/w13243533

Stevens-Rumann, C. S., & Morgan, P. (2019). Tree regeneration following wildfires in the Western US: A review. *Fire Ecology*, *15*(1), 15. https://doi.org/10.1186/s42408-019-0032-1

Sturm, M., Goldstein, M. A., & Parr, C. (2017). Water and life from snow: A trillion dollar science question. *Water Resources Research*, *53*(5), 3534–3544. https://doi.org/10.1002/2017WR020840

Trujillo, E., Ramírez, J. A., & Elder, K. J. (2007). Topographic, meteorologic, and canopy controls on the scaling characteristics of the spatial distribution of snow depth fields. *Water Resources Research*, *43*(7), W07409. https://doi.org/10.1029/2006WR005317

Uecker, T. M., Kaspari, S. D., Musselman, K. N., & Skiles, S. M. (2020). The post-wildfire impact of burn severity and age on black carbon snow deposition and implications for snow water resources, cascade range, Washington. *Journal of Hydrometeorology*, *21*(8), 1777–1792. https://doi.org/10.1175/JHM-D-20-0010.1

Viviroli, D., Dürr, H. H., Messerli, B., Meybeck, M., & Weingartner, R. (2007). Mountains of the world, water towers for humanity: Typology, mapping, and global significance. *Water Resources Research*, *43*(7), W07447. https://doi.org/10.1029/2006WR005653

Wagner, A. M., Bennett, K. E., Liston, G. E., Hiemstra, C. A., & Cooley, D. (2021). Multiple indicators of extreme changes in snow-dominated streamflow regimes, Yakima River basin region, USA. *Water (Switzerland)*, *13*(19), 2608. https://doi.org/10.3390/w13192608

Webb, R., Litvak, M., & Brooks, P. D. (2023). The role of terrain-mediated hydroclimate in vegetation recovery after wildfire. *Environmental Research Letters*, *18*(6), 064036. https://doi.org/10.1088/1748-9326/acd803

Westerling, A. L., Hidalgo, H. G., Cayan, D. R., & Swetnam, T. W. (2006). Warming and earlier spring increase Western U.S. forest wildfire activity. *Science*, *313*(5789), 940–943. https://doi.org/10.1126/science.1128834

Westerling, A. L., Turner, M. G., Smithwick, E. A. H., Romme, W. H., & Ryan, M. G. (2011). Continued warming could transform greater Yellowstone fire regimes by mid-21st century. *Proceedings of the National Academy of Sciences of the United States of America*, *108*(32), 13165–13170. https://doi.org/10.1073/pnas.1110199108

Westerling, A. L. R. (2016). Increasing Western US forest wildfire activity: Sensitivity to changes in the timing of spring. *Philosophical Transactions of the Royal Society B: Biological Sciences*, *371*(1696), 20150178. https://doi.org/10.1098/rstb.2015.0178

Wrzesien, M. L., Durand, M. T., Pavelsky, T. M., Kapnick, S. B., Zhang, Y., Guo, J., & Shum, C. K. (2018). A New Estimate of North American Mountain Snow Accumulation From Regional Climate Model Simulations. *Geophysical Research Letters*, *45*(3), 1423–1432. https://doi.org/10.1002/2017GL076664